

RESEARCH ARTICLE | JULY 14 2022

The role of Nb₂O₅ deposition process on perovskite solar cells

Silvia L. Fernandes ; Larissa de O. Garcia; Roberto de A. Ramos Júnior ; Lucas J. Affonso ; Diego Bagnis ; Rodrigo Vilaça; Fenelon M. Pontes ; José H. D. da Silva ; Carlos F. O. Graeff 



Journal of Renewable and Sustainable Energy 14, 043703 (2022)

<https://doi.org/10.1063/5.0083073>




View
Online



Export
Citation

CrossMark



APL Energy
Bridging basic research and innovative technology that will impact the future

First Articles Coming Soon!
No Article Processing Charges (APCs) through 2023



The role of Nb₂O₅ deposition process on perovskite solar cells

Cite as: J. Renewable Sustainable Energy **14**, 043703 (2022); doi: 10.1063/5.0083073

Submitted: 21 December 2021 · Accepted: 19 June 2022 ·

Published Online: 14 July 2022



View Online



Export Citation



CrossMark

Silvia L. Fernandes,^{1,2,a)}  Larissa de O. Garcia,^{1,3}  Roberto de A. Ramos Júnior,³  Lucas J. Affonço,³  Diego Bagnis,²  Rodrigo Vilaça,²  Fenelon M. Pontes,^{3,4}  José H. D. da Silva,^{1,3}  and Carlos F. O. Graeff^{1,3} 

AFFILIATIONS

¹School of Sciences, Department of Physics, São Paulo State University (UNESP), Bauru, SP 17033-360, Brazil

²Centro de Inovações CSEM Brasil, Belo Horizonte, MG 31035-536, Brazil

³School of Sciences, POSMAT-Post-Graduate Program in Materials Science and Technology, São Paulo State University (UNESP), Bauru, SP 17033-360, Brazil

⁴School of Sciences, Department of Chemicals, São Paulo State University (UNESP), Bauru, SP 17033-360, Brazil

a) Author to whom correspondence should be addressed: sy.fernandes@hotmail.com

ABSTRACT

Two different methods are used to deposit Nb₂O₅ as compact electron transport layers in n-i-p double cation mixed-halide perovskite Cs_{0.17}FA_{0.83}Pb(I_{0.83}Br_{0.17})₃ solar cells: reactive sputtering and spin coating. These different Nb₂O₅ films influenced perovskite growth and the charge transport in the cells. Photovoltaic parameters were obtained with an average power conversion efficiency of 17.0% and 15.7% for the devices based on sputtered and spin-coated Nb₂O₅, respectively. The mobility and the extracted charges were higher in sputtered Nb₂O₅-based devices than in the spin-coated ones. This effect is attributed to the larger grain sizes observed in the perovskite films when deposited onto the sputtered Nb₂O₅ layers. The higher densities of grain boundaries in the spin-coated Nb₂O₅-based devices increase ion diffusion and are expected to decrease efficiency.

Published under an exclusive license by AIP Publishing. <https://doi.org/10.1063/5.0083073>

I. INTRODUCTION

Perovskite solar cells (PSCs) are considered a promising technology due to their high efficiency and low production cost.¹ Since the first report of solid-state PSCs in 2012,² which had a power conversion efficiency (PCE) of 9.7% and 500 h of stability, intensive efforts resulted in the increase in cell efficiency, reaching 25.7% in 2021.³

In PSCs, Electron Transport Layers (ETLs) are crucial in extracting and transporting photogenerated electrons. The properties of a good ETL include high charge mobility and conduction band alignment with the perovskite. TiO₂ is the most used ETL in n-i-p devices; however, the material presents limitations in terms of stability and efficiency due to its oxygen vacancy defects, which are responsible for electron-hole recombination and degradation.^{4–6} Nb₂O₅ is an interesting alternative ETL for PSCs due to its good electronic energy level alignment, higher stability, and lower photoactivity compared to TiO₂.^{7–9} In a previous work,¹⁰ our group obtained methylammonium lead iodide PSCs with negligible J–V hysteresis using mesoporous TiO₂ over a Nb₂O₅ compact layer deposited by sputtering. Ling *et al.* also used radio frequency sputtered Nb₂O₅ without any post-treatment and reached a PCE of 18%. Using simpler deposition

methods, Shen *et al.*¹¹ reached 17.4% efficiency in mesoscopic layered devices and 19.2% for planar PSCs using sol-gel Nb₂O₅ films.

Perovskite crystallization is strongly dependent on the material in which it is deposited. For instance, Liu *et al.*^{12–16} showed that by increasing perovskite grain size, the photovoltaic performance is improved. In another recent work,¹⁷ the role of grain boundaries (GBs) in PSCs was discussed, concluding that small grains are recombination hot spots in PSCs.

In this report, the influence of spin-coated vs sputtered Nb₂O₅ in association with mesoporous TiO₂ ETLs on PSCs is investigated. In both the methods, efficient PSCs were produced; however, the mobility and the charge extraction were found to be higher in sputtered Nb₂O₅ based PSCs, attributed to the resultant larger perovskite (PVK) crystal grains obtained.

II. METHODOLOGY

A. Materials

Ultra-dry lead (II) iodide 99.999% (PbI₂) was purchased from TCI Chemicals, lead (II) bromide 99.998% (PbBr₂), cesium iodide 99.999% (CsI), niobium (V) ethoxide 99.95%, anhydrous dimethyl

sulfoxide (DMSO) $\geq 99.9\%$, anhydrous dimethylformamide (DMF) 99.8%, anhydrous chlorobenzene (CB) 99.8%, and anhydrous acetonitrile 99.8% were purchased from Sigma Aldrich. Formamidinium iodide (FAI), formamidinium bromide (FABr), and TiO_2 paste (30 NR-D) were purchased from Greatcell Solar, and ethanol 99.8% was purchased from Neon. All reagents listed in this section were used without any further purification.

B. Compact Nb_2O_5 films preparation

Nb_2O_5 solution was prepared following the method reported by Shen *et al.*⁹ For this, a solution of 25 μl of niobium ethoxide, 2 ml of ethanol, and 40 μl of hydrochloric acid (2 M) was prepared. After 2 h of stirring at room temperature, the precursor solution was spin-coated on clean Fluorine-doped Tin Oxide (FTO) substrates at 4000 rpm for 30 s with an acceleration of 500 rpm s^{-1} , followed by pre-drying at 100 °C for 10 min. The spin-coated (SC) Nb_2O_5 films were named Nb_2O_5 -SC.

Nb_2O_5 films were deposited by reactive magnetron sputtering using a target of metallic Nb with 3" of diameter (99.9% purity) in a Kurt J. Lesker System. The deposition temperature and plasma power were 500 °C and 240 W, respectively. The chamber pressure was kept in 5.0×10^{-3} Torr by a 40 sccm of high purity argon flow and 3.5 sccm oxygen flow. The deposition time was 3 min to obtain films of ~ 100 nm of thickness, comparable with the one deposited by spin coating. The reactive sputtered (RS) films were named Nb_2O_5 -RS.

C. Perovskite preparation

Double-cation mixed-halide perovskite solution was prepared by dissolving PbI_2 (1.2 mmol), FAI (1 mmol), and CsI (0.2 mmol) in a 4:1 (v/v) mixture of DMF: DMSO. Then, the second solution of PbBr_2 (1.2 mmol) and FAI (1.2 mmol) in 4:1 (v/v) DMF: DMSO was prepared. The two solutions were stirred overnight at 70 °C. Afterwards, the solutions were mixed to obtain a FAPbBr_3 : CsFAPbI_3 (17:83% v/v) solution. The precursor solution of $\text{Cs}_{0.17}\text{FA}_{0.83}\text{Pb}(\text{I}_{0.83}\text{Br}_{0.17})_3$ was filtered through a 0.45 μm syringe filter.

D. Device fabrication

Fluorine-doped Tin Oxide (FTO) on glass (2.2 mm, 7–8 Ω/Sq FTO TEC 7 Coated) was patterned by etching with Zn powder and concentrated HCl. Then, the substrates were cleaned, with Extran[®] (50% v/v in H_2O), de-ionized water, acetone, and 2-propanol for 20 min each in an ultrasound bath. Next, the substrates were dried with N_2 . The Nb_2O_5 films were deposited on FTO as described in Sec. II C. The mesoporous TiO_2 layer was deposited on top of the Nb_2O_5 compact layer by spin-coating a solution of 150 mg/ml in ethanol of a commercial TiO_2 paste at 3000 rpm for 30 s. Compact and mesoporous layers were thermally annealed at 550 °C for 60 min. Nb_2O_5 -RS with mesoporous TiO_2 on top are named ETL-RS, and the same for Nb_2O_5 -SC with mesoporous TiO_2 , ETL-SC.

Perovskite films were spin-coated at 1000 rpm for 10 s, followed by 6000 rpm for 25 s. Five seconds before the end of the spinning, 200 μl of CB as an anti-solvent was dropped. Then, a Spiro-OMeTAD solution (73 mg/ml in CB) doped with 29 μl of 4-tert-butyl pyridine, 29 μl of FK209 cobalt complex solution (300 mg/ml in acetonitrile), and 18 μl of lithium bis(trifluoromethanesulfonic)imide (Li-TFSI) solution (520 mg/ml in acetonitrile) was spin-coated on the perovskite

film using 4000 rpm for 60 s. Finally, 80 nm of Au electrode was thermally evaporated at the top of the device at a rate of 0.2 $\text{\AA}/\text{s}$ in the first 5 nm and 1 $\text{\AA}/\text{s}$ in the remaining 75 nm using a HHV auto 306 evaporator system with Inficon SQM-160 thickness control.

E. Characterization

The devices were characterized by x-ray diffraction (XRD) using a Rigaku MiniFlex 600 diffractometer (Cu $K\alpha$ radiation with $\lambda = 1.5406 \text{\AA}$). Field Emission Gun Scanning Electron Microscopy (FEG-SEM) and Atomic Force Microscopy (AFM) images were taken from three different points in an area of 16 μm^2 and analyzed using JEOL JSM-7500F and the PC-SEM and Park XE7 software, respectively. The average grain sizes of PVK were calculated using the SEM images (50 000 magnification) through the ImageJ software, and the crystallite sizes using Scherrer's equation. External Quantum Efficiency (EQE) measurements were made with a PTS-2-QE Quantum Efficiency/IPCE System from Sciencetech. Contact angle measurements were carried using Ossila Contact Angle Goniometer. The measurements were made using the PVK precursor solution in DMF: DMSO (4:1 v/v), the same used to film deposition.

Current density–voltage (J–V) curves of the devices were obtained through a Keithley 2400 digital source meter under the illumination of AM 1.5G spectrum obtained by a solar simulator from Newport (Class AAA, 94023A-U) with a power of 100 mW cm^{-2} and calibrated with certified silicon solar cell before the measurements. Charge extraction in a linearly increased voltage (CELIV) and photo-CELIV was measured with Paivos equipment from Fluxin, using a ramp of 10^4 V/s and final potential of 0.5 V. Impedance spectroscopy was obtained using Metrohm Autolab PGSTAT302 equipped with a FRA32 impedance module.

III. RESULTS

A. Morphological and structural analyses

The crystallization of perovskite films is known to be extremely sensitive to small changes in the deposition conditions, including the material over which the film is deposited, as reported.^{5,18,19} Figures 1(a)–1(d) show the top-view SEM images of Nb_2O_5 and PVK films. From Nb_2O_5 microscopies, it can be observed that both films are composed of nanometric particles, as shown in Figs. 1(a) and 1(c). The PVK films are uniform and compact. However, larger grain sizes are found for the ones grown on ETL-RS. Average grain sizes of 443 ± 6 and 300 ± 7 nm were calculated for the films grown on ETL-RS and ETL-SC, respectively.

The contact angles of PVK solution on ETL-RS and ETL-SC are presented in Table I. Wettability is known to be important in PVK crystallization, larger grains are associated with high wettability.^{20,21} A smaller contact angle or better wettability is found in ETL-RS compared to ETL-SC, in agreement with its larger PVK grain sizes.

The Nb_2O_5 and PVK films roughness were also evaluated by AFM, see Fig. 2. The Nb_2O_5 -RS film roughness is 28.5 ± 0.4 nm, close to the one found in Nb_2O_5 -SC, 29.8 ± 0.5 nm. The RMS roughness of the PVK grown on ETL-RS is clearly smaller than that on ETL-SC, 29.4 ± 0.3 and 39.0 ± 0.4 nm, respectively. The smaller roughness of PVK on ETL-RS is associated with the larger grains, as discussed previously.

All samples have high crystallinity, independent of the compact layer used,^{22,23} as indicated in Fig. S1. The diffraction peak at 12.7°

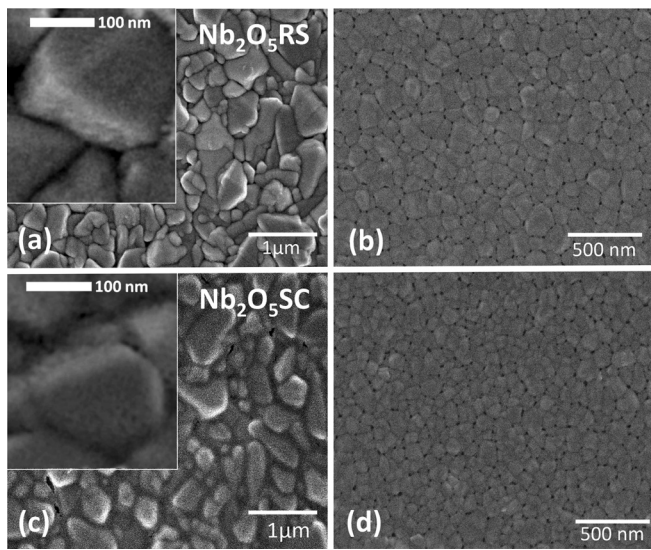


FIG. 1. SEM images with 50 000 magnification of (a) Nb₂O₅-RS, (b) PVK on ETL-RS, (c) Nb₂O₅-SC, and (d) PVK on ETL-SC.

TABLE I. Measured contact angles of PVK solution on ETL-RS and ETL-SC.

Sample	Liquid	Left contact angle	Right contact angle	Average
ETL-RS	PVK solution	14.5	12.5	13.5
ETL-SC	PVK solution	27.3	30.7	29.0

found in all samples is attributed to traces of PbI₂ not converted into perovskite.^{22,23} The crystallite sizes (Table S1) were estimated using Scherrer's equation applied to the (012), (022), and (003) planes. The values found are 42 ± 4 nm for PVK on Nb₂O₅-RS and 31 ± 3 nm for PVK on Nb₂O₅-SC.

B. Electrical characterization

J-V curves of PSCs using the different ETLs are presented in Fig. 3. The key parameters, including short-circuit current density (J_{sc}), open-circuit voltage (V_{oc}), fill factor (FF), and power conversion efficiency (PCE), are presented in Fig. 4 and Table II as well as the Hysteresis Index (HI). ETL-RS devices have average PCE of 17.0%, with $J_{sc} = 22.04$ mA/cm², $V_{oc} = 1.05$ V, and FF = 73%, in reverse

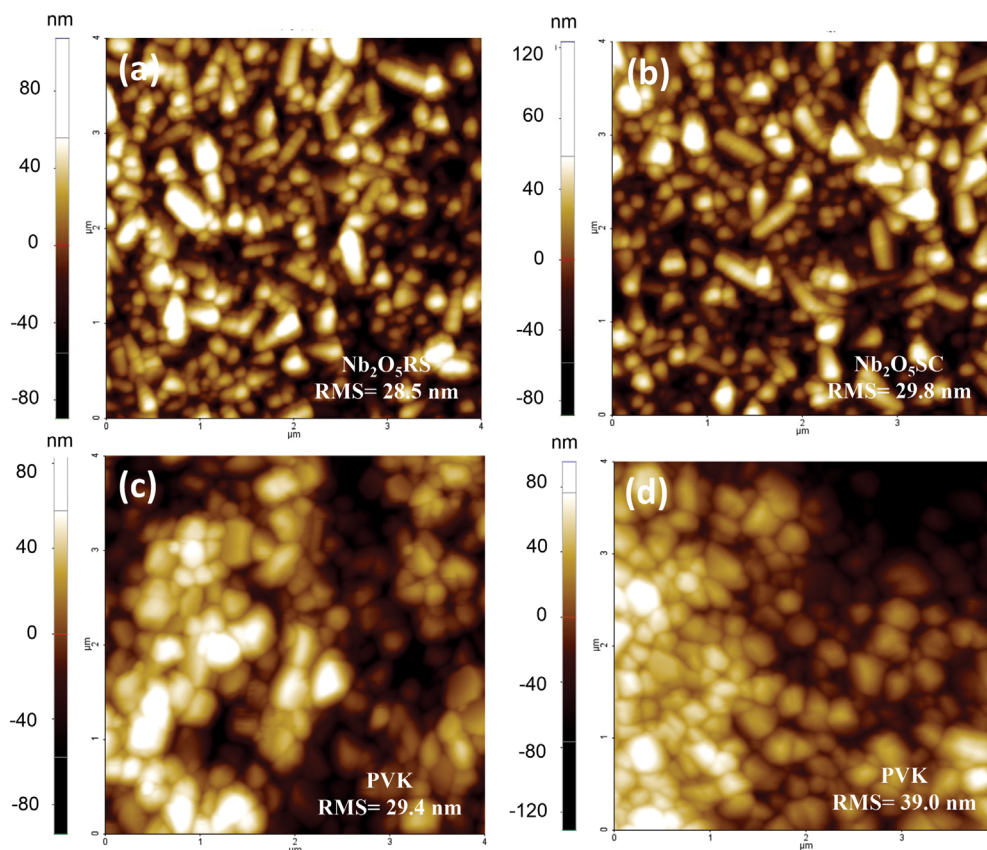


FIG. 2. AFM images of (a) surface of Nb₂O₅-RS film, (b) surface of Nb₂O₅-SC film, (c) surface of PVK on top of ETL-RS, and (d) surface of PVK on top of ETL-SC films. The ordinates are measured in nanometers while the abscissas are in micrometers. The insets show the measured roughness of each surface.

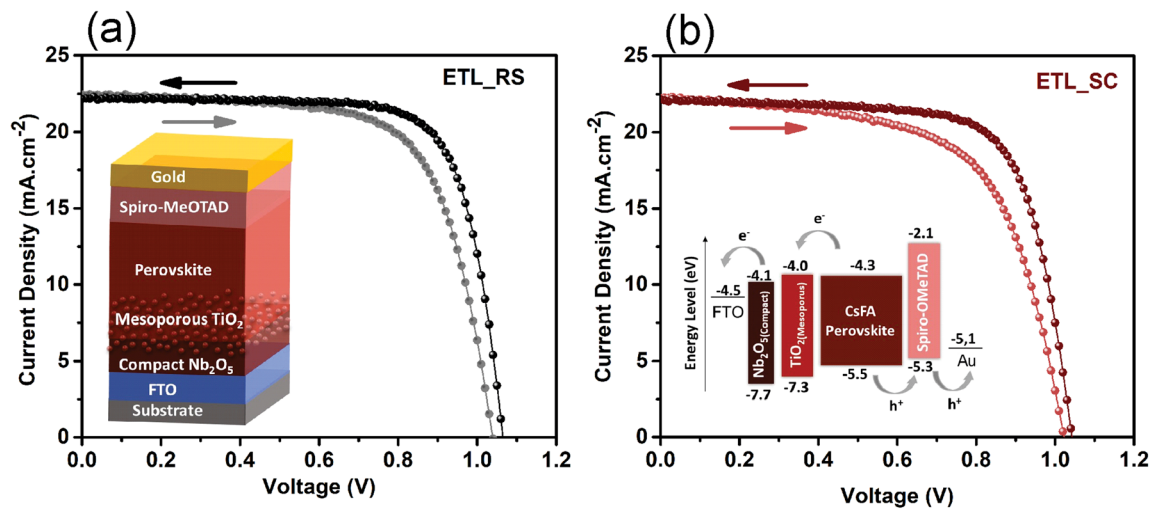


FIG. 3. J-V curves of (a) Nb₂O₅-RS and (b) Nb₂O₅-SC based PSCs, the scan direction of each curve is indicated by the arrows with the same color of the curves. The insets show the structure of the devices as well as the band diagram.

scan. In forward scan, the PCE is 16.4%, J_{sc} 22.16 mA/cm², V_{oc} 1.05 V, and FF 70%. For ETL-SC devices, PCE is 15.7%, J_{sc} 22.19 mA/cm², V_{oc} 1.02 V, and FF 69% in reverse scan. In forward scan, PCE is 14.1%, J_{sc} 22.34 mA/cm², V_{oc} 1.00 V, and FF 62%. The parameters are similar for both devices, but slightly better for ETL-RS PSCs. The best curves are shown in Fig. S2 and their parameters in Table S2. When ETL-SC is used, the HI obtained from $HI = \frac{PCE_{Reverse} - PCE_{Forward}}{PCE_{Reverse}}$ ²⁴ is increased by a

factor of 1.5, from 0.097 for ETL-RS to 0.140 for ETL-SC based PSCs. The external quantum efficiency (EQE) of the devices, shown in Fig. S3, has no significant differences among the different devices.

Charge Extraction by Linearly Increasing Voltage (CELIV) and photo-CELIV were carried out. From Photo-CELIV, the ETL-RS based PSCs has better charge extraction, as shown in Fig. 5. Even though the current transients are similar, j_{max} is higher in ETL-RS.

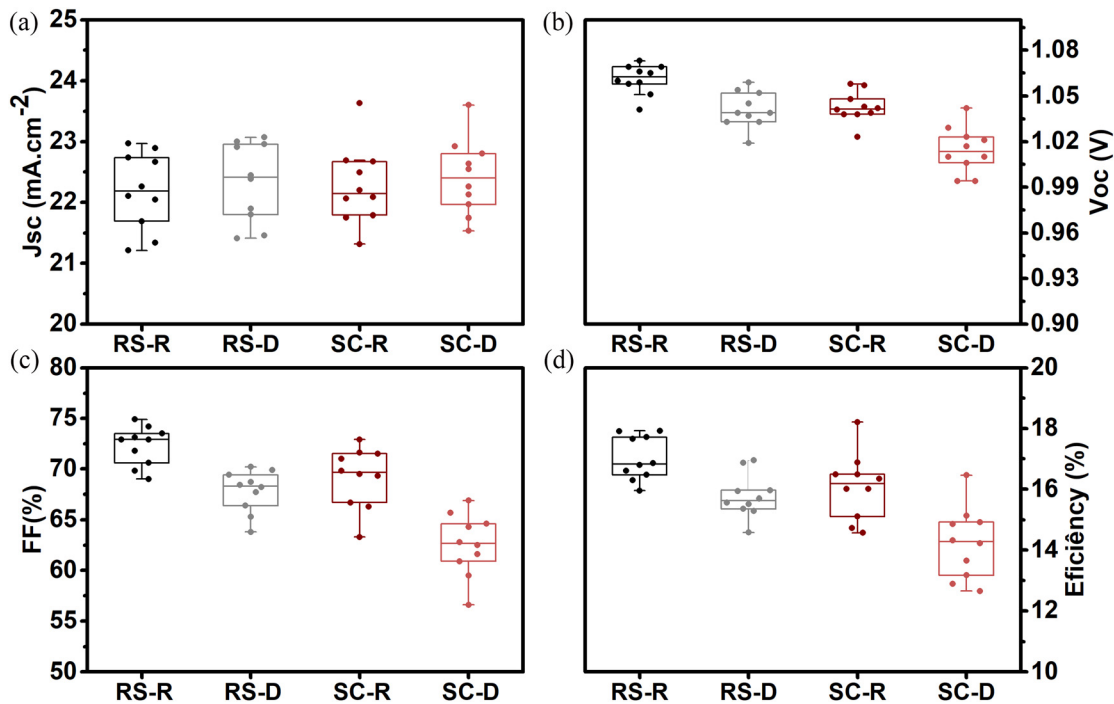


FIG. 4. Statistics of (a) J_{sc} , (b) V_{oc} , (c) FF, and (d) PCE of the different PSCs analyzed. These results are for measurements in forward and reverse scan directions.

TABLE II. PSCs parameters extracted from J–V curves; the line corresponding to the “best curve” refers to the parameters extracted from Fig. S3.

	J_{sc} (mA cm^{-2})	V_{oc} (V)	FF (%)	PCE (%)	HI (#)
Nb₂O₅-RS					
Reverse	22.0 ± 0.9	1.05 ± 0.02	73 ± 2	17.00 ± 0.90	0.10 ± 0.07
Best curve	23.1	1.05	74.2	18.0	
Forward	22.2 ± 0.9	1.05 ± 0.01	70 ± 1	16.00 ± 1.00	
Best curve	23.4	1.06	74.7	18.6	
Nb₂O₅-SC					
Reverse	22.2 ± 0.9	1.02 ± 0.03	69 ± 4	16.00 ± 1.00	0.13 ± 0.07
Best curve	23.0	1.04	72.5	17.3	
Forward	22.3 ± 0.8	1.00 ± 0.04	63 ± 5	14.00 ± 2.00	
Best curve	23.3	1.05	71.5	17.5	

ETL-RS devices have also higher mobility, $2.45 \times 10^{-2} \text{ cm}^2/\text{V s}$, compared to $2.06 \times 10^{-2} \text{ cm}^2/\text{V s}$ for ETL-SC.

Normalized photo-CELIV as a function of light intensity is shown in Fig. 6(a). For this figure, the CELIV was subtracted from the photo-CELIV, to ensure that the response is only related to photogenerated charge carriers. The transient peak of both samples narrows as the light intensity increase, attributed to a decrease in dispersive transport. As shown in Fig. 6(b), the carrier’s mobility of ETL-SC devices decreases in the lower light intensities regime until it stabilizes at about 50 mW/cm^2 and higher. This trend is unusual; however, it has been observed in other materials. For instance, in InSe, the decrease was attributed to an increase in the drift barrier height, i.e., the potential barrier between grains, due to the capture of carriers by fast recombination centers.²⁵ On the other hand, the mobility of ETL-RS increased slightly with light intensity. In Fig. 6(c), the extracted charge as function of light intensity is shown

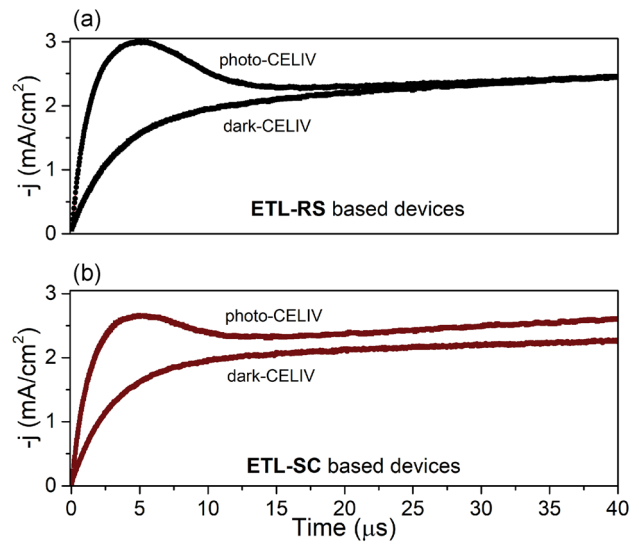


FIG. 5. CELIV and photo-CELIV of (a) ETL-RS and (b) ETL-SC based PSC. The ramp used was 10^4 V/s and the final applied voltage potential was 0.5 V .

for both samples indicating higher extraction on ETL-RS based PSCs, in particular at higher intensities.

Figure 7 shows the normalized photo-CELIV using different delay times between the light pulse and the start of the voltage ramp. As can be seen in the figure, the transport in ETL-RS PSCs is less dispersive (narrower peaks). However, the mobilities are similar, as shown in the insets of Fig. 7(a). The extracted charge, as a function of delay time, is shown in Fig. 7(b). The curves were fitted by a double exponential decay function $n(t) = n_0 \exp(-t/\tau_1) + n'_0 \exp(-t/\tau_2)$, where τ_1 and τ_2 are the recombination times. The double exponential fitting is an indication of distinct recombination centers, with different

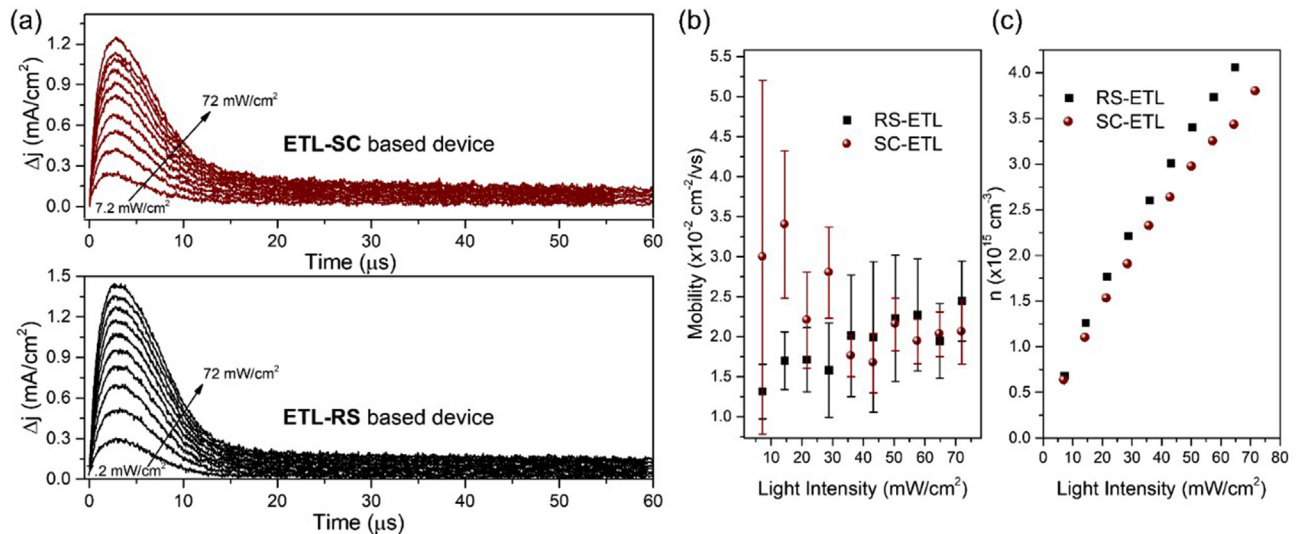


FIG. 6. (a) Photo-CELIV transients varying the light intensity for ETL-SC PSCs (top panel) and ETL-RS (bottom panel); (b) extracted charge as a function of light intensity and (c) mobility as a function of light intensity.

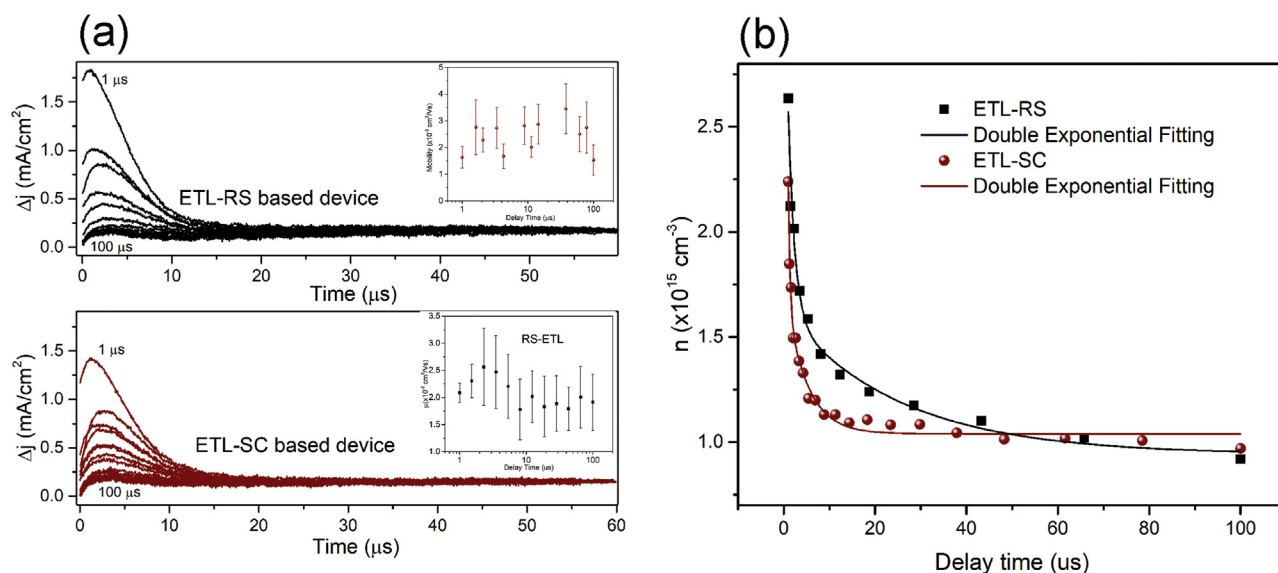


FIG. 7. (a) Photo-CELIV transients with varying delay times between the light pulse and the voltage ramp, for the different PSCs. The inset shows the mobility as a function of delay time. (b) Fitted charge extracted as a function of delay time for the different devices analyzed.

characteristic times. The fitting parameters are shown in Table S3. The τ_1 and τ_2 of ETL-RS PSCs are higher, 1.4 ± 0.4 and $25 \pm 12 \mu\text{s}$, compared to 1 ± 2 and $4.6 \pm 0.9 \mu\text{s}$ from ETL-SC.

Figure 8 shows the capacitance of the different devices measured from impedance in the dark. C-f is used to better understand charge accumulation.²⁶ At low-frequencies, $<10^2$ Hz, ETL-SC PSCs capacitance is higher, indicating elevated ion diffusion in this PSC.²⁶ Notice that the capacitance drops at higher frequencies in ETL-RS PSC.

C. Discussion

As discussed earlier, the crystallization of hybrid lead halide perovskites is very sensitive to the deposition process.^{19,27–29} Our results show that though PVK is grown on top of a mesoporous layer, the

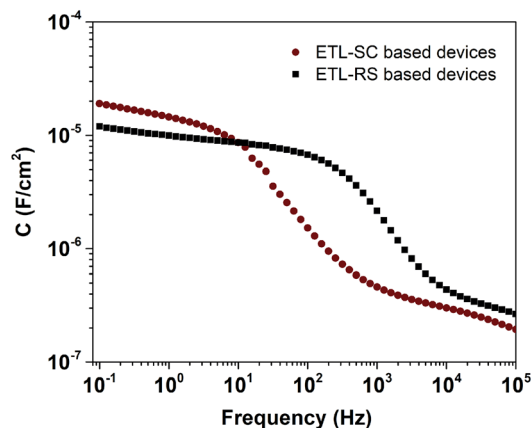


FIG. 8. Impedance spectroscopy of PSCs in the dark for the different PSCs analyzed.

Nb_2O_5 underlayer influences the crystal growth or the crystal grain size. We believe that the pores on TiO_2 films, Fig. S4, are responsible for this effect. Through the pores, the PVK precursor solution infiltrates reaching the compact layer. Wettability is most probably responsible for the increase in grain size and is dominated by the substrate. Considering that the perovskite precursors are soluble in a polar solvent, such as DMF, the precursors show a strong affinity for hydrophilic surfaces.³⁰ Therefore, hydrophobic substrates may induce a noncontinuous perovskite layer or lead to pinholes formation due to poor wetting. In our case, the difference in wettability may come from the higher purity of the Nb_2O_5 grown by sputtering deposition.

CELIV and photo-CELIV results, Figs. 5 and 6, showed that the mobility and charge extraction are higher in ETL-RS PSCs. The grain size may be responsible for this effect.^{31,32} Bigger grains are related to fewer grain boundaries (GBs) that are known to be defect-rich.^{17,33–35} In addition, as expected, the ion diffusion observed in the low-frequency range (~ 10 – 100 Hz), Fig. 8, is higher in ETL-SC PSCs.³³ Ion diffusion is normally associated with non-radiative recombination.³⁶ Our results corroborate that, see Fig. 7.

With regard to the capacitance measurements, Fig. 8, in the model of Almora,⁴² the drop in capacitance is associated with the balance in the occupation of deep and shallow traps. Our results show that Nb_2O_5 -SC PSC has a capacitance drop at lower frequencies, $\sim 10^3$ Hz, indicating that the defects are deeper in this device.^{37–41}

As a final comment, although both techniques can be used in large-scale production, solution-based deposition are associated with lower costs and are easier to implement.

IV. CONCLUSIONS

The use of different Nb_2O_5 -ETL compact layer deposition processes was found to influence the performance of double cation mixed-halide $\text{Cs}_{0.17}\text{FA}_{0.83}\text{Pb}(\text{I}_{0.83}\text{Br}_{0.17})_3$ solar cells. It was observed that the crystal grain size and perovskite film morphology are

influenced by the ETL compact layer. In particular, the Nb₂O₅ compact layer grown by RF-sputtering had higher wettability resulting in PVK with larger grain sizes. The mesoporous TiO₂ layer between PVK and Nb₂O₅ films was found to have little impact on the effect. In sputtered compact layer PSCs, the charge mobility and extraction are found to be higher.

SUPPLEMENTARY MATERIAL

See the [supplementary material](#) for additional characterizations such as SEM, XRD and mean crystallite size, EQE, best J–V curves, and photo-CELIV parameters.

ACKNOWLEDGMENTS

This work was supported by São Paulo Research Foundation-FAPESP (research Projects No. 2020/04905-1 and 2020/12356-8) and the Center for the Development of Functional Materials-CEPID (No. 13/07296-2).

AUTHOR DECLARATIONS

Conflict of Interest

The authors have no conflicts to disclose.

Author Contributions

Silvia Leticia Fernandes: Conceptualization (equal); Data curation (equal); Investigation (equal); Methodology (equal); Project administration (equal); Supervision (equal); Writing – original draft (equal); Writing – review and editing (equal). **Larissa de Oliveira Garcia:** Conceptualization (equal); Data curation (equal); Methodology (equal); Writing – original draft (equal). **Roberto de Aguiar Ramos Jr.:** Data curation (equal); Methodology (equal); Software (equal); Writing – review and editing (equal). **Lucas Jorge Affonso:** Data curation (equal); Formal analysis (equal); Writing – original draft (equal). **Diego Bagnis:** Writing – original draft (equal); Writing – review and editing (lead). **Rodrigo Vilaca:** Resources (equal); Writing – original draft (equal); Writing – review and editing (equal). **Fenelon Martinho Pontes:** Conceptualization (equal); Methodology (equal); Writing – original draft (equal); Writing – review and editing (equal). **Jose Humberto Dias da Silva:** Conceptualization (equal); Investigation (equal); Writing – original draft (equal); Writing – review and editing (equal). **Carlos F.O. Graeff:** Conceptualization (equal); Funding acquisition (equal); Investigation (equal); Project administration (equal); Resources (equal); Writing – original draft (equal); Writing – review and editing (lead).

DATA AVAILABILITY

The data that support the findings of this study are available within the article and its [supplementary material](#).

REFERENCES

- X. Shi, Y. Wu, J. Chen, M. Cai, Y. Yang, X. Liu, Y. Tao, M. Guli, Y. Ding, and S. Dai, *J. Mater. Chem. A* **8**, 7205 (2020).
- H. S. Kim, C. R. Lee, J. H. Im, K. B. Lee, T. Moehl, A. Marchioro, S. J. Moon, R. Humphry-Baker, J. H. Yum, J. E. Moser, M. Grätzel, and N. G. Park, *Sci. Rep.* **2**, 1 (2012).
- NREL, Best Research-Cell Efficiency Chart, <https://www.nrel.gov/pv/cell-efficiency.html> (accessed April 01, 2022).
- K. Mahmood, S. Sarwar, and M. T. Mehran, *RSC Adv.* **7**, 17044 (2017).
- M. I. H. Ansare, A. Qurashi, and M. K. Nazeeruddin, *J. Photochem. Photobiol. C* **35**, 1 (2018).
- H. S. Rao, B. X. Chen, W. G. Li, Y. F. Xu, H. Y. Chen, D. Bin Kuang, and C. Y. Su, *Adv. Funct. Mater.* **25**, 7200 (2015).
- M. A. Aegerter, *Sol. Energy Mater. Sol. Cells* **68**, 401 (2001).
- K. Hamada, N. Murakami, T. Tsubota, and T. Ohno, *Chem. Phys. Lett.* **586**, 81 (2013).
- X. Ling, J. Yuan, D. Liu, Y. Wang, Y. Zhang, S. Chen, H. Wu, F. Jin, F. Wu, G. Shi, X. Tang, J. Zheng, S. Liu, Z. Liu, and W. Ma, *ACS Appl. Mater. Interfaces* **9**, 23181 (2017).
- S. L. Fernandes, A. C. Véron, N. F. A. Neto, F. A. Nüesch, J. H. Dias da Silva, M. A. Zaghete, and F. D. O. Carlos, *Mater. Lett.* **181**, 103 (2016).
- D. Shen, W. Zhang, Y. Li, A. Abate, and M. Wei, *ACS Appl. Nano Mater.* **1**, 4101 (2018).
- T. Niu, J. Lu, R. Munir, J. Li, D. Barrit, X. Zhang, H. Hu, Z. Yang, A. Amassian, K. Zhao, and S. (Frank) Liu, *Adv. Mater.* **30**, 1706576 (2018).
- Z. Liu, F. Cao, M. Wang, M. Wang, and L. Li, *Angew. Chem., Int. Ed.* **59**, 4161 (2020).
- H. Tsai, W. Nie, P. Cheruku, N. H. Mack, P. Xu, G. Gupta, A. D. Mohite, and H.-L. Wang, *Chem. Mater.* **27**, 46 (2015).
- X. Ren, Z. Yang, D. Yang, X. Zhang, D. Cui, Y. Liu, Q. Wei, H. Fan, and S. F. Liu, *Nanoscale* **8**, 3816 (2016).
- W. Xu, G. Lei, C. Tao, J. Zhang, X. Liu, X. Xu, W.-Y. Lai, F. Gao, and W. Huang, *Adv. Funct. Mater.* **28**, 1802320 (2018).
- Q. An, F. Paulus, D. Becker-Koch, C. Cho, Q. Sun, A. Weu, S. Bitton, N. Tessler, and Y. Vaynzof, *Matter* **4**, 1683 (2021).
- X. Lin, D. Cui, X. Luo, C. Zhang, Q. Han, Y. Wang, and L. Han, *Energy Environ. Sci.* **13**, 3823 (2020).
- E. Climent-Pascual, B. C. Hames, J. S. Moreno-Ramírez, A. L. Álvarez, E. J. Juárez-Pérez, E. Mas-Marza, I. Mora-Seró, A. De Andrés, and C. Coya, *J. Mater. Chem. A* **4**, 18153 (2016).
- S. You, H. Wang, S. Bi, J. Zhou, L. Qin, X. Qiu, Z. Zhao, Y. Xu, Y. Zhang, X. Shi, H. Zhou, and Z. Tang, *Adv. Mater.* **30**, 1706924 (2018).
- M. Zhang, W. Zhou, W. Hu, B. Li, Q. Qiao, and S. Yang, *ACS Appl. Mater. Interfaces* **12**, 12696 (2020).
- T. J. Jacobsson, J. P. Correa-Baena, E. Halvani Anaraki, B. Philippe, S. D. Stranks, M. E. F. Bouduban, W. Tress, K. Schenk, J. Teuscher, J. E. Moser, H. Rensmo, and A. Hagfeldt, *J. Am. Chem. Soc.* **138**, 10331 (2016).
- S. Svanström, T. J. Jacobsson, T. Sloboda, E. Giangrisostomi, R. Ovsyannikov, H. Rensmo, and U. B. Cappel, *J. Mater. Chem. A* **6**, 22134 (2018).
- S. N. Habisreutinger, N. K. Noel, and H. J. Snaith, *ACS Energy Lett.* **3**, 2472 (2018).
- A. S. Abidinov, R. F. Babayeva, S. I. Amirova, N. A. Ragimova, and R. M. Rzaev, *Semiconductors* **48**, 981–985 (2014).
- P. Lopez-Varo, J. A. Jiménez-Tejada, M. García-Rosell, S. Ravishankar, G. García-Belmonte, J. Bisquert, and O. Almora, *Adv. Energy Mater.* **8**, 1 (2018).
- M. De Bastiani, V. D’Innocenzo, S. D. Stranks, H. J. Snaith, and A. Petrozza, *APL Mater.* **2**, 081509 (2014).
- H. Zhang, C. Zhao, D. Li, H. Guo, F. Liao, W. Cao, X. Niu, and Y. Zhao, *J. Mater. Chem. A* **7**, 2804 (2019).
- X. Niu, N. Li, Q. Chen, and H. Zhou, *Adv. Energy Sustainable Res.* **2**, 2000046 (2021).
- M. Abbas, L. Zeng, F. Guo, M. Rauf, X. C. Yuan, and B. Cai, *Materials* **13**, 4851 (2020).
- Z. Chu, M. Yang, P. Schulz, D. Wu, X. Ma, E. Seifert, L. Sun, X. Li, K. Zhu, and K. Lai, *Nat. Commun.* **8**, 2230 (2017).
- H. Do Kim, H. Ohkita, H. Benten, and S. Ito, *Adv. Mater.* **28**, 917 (2016).
- Y. Shao, Y. Fang, T. Li, Q. Wang, Q. Dong, Y. Deng, Y. Yuan, H. Wei, M. Wang, A. Gruverman, J. Shield, and J. Huang, *Energy Environ. Sci.* **9**, 1752 (2016).
- P. Cui, P. Fu, D. Wei, M. Li, D. Song, X. Yue, Y. Li, Z. Zhang, Y. Li, and J. M. Mbengue, *RSC Adv.* **5**, 75622 (2015).
- X. Wu, M. T. Trinh, D. Niesner, H. Zhu, Z. Norman, J. S. Owen, O. Yaffe, B. J. Kudisch, and X.-Y. Zhu, *J. Am. Chem. Soc.* **137**, 2089 (2015).

- ³⁶D. A. Jacobs, H. Shen, F. Pfeffer, J. Peng, T. P. White, F. J. Beck, and K. R. Catchpole, *J. Appl. Phys.* **124**, 225702 (2018).
- ³⁷T. S. Sherkar, C. Momblona, L. Gil-Escrig, J. Ávila, M. Sessolo, H. J. Bolink, and L. J. A. Koster, *ACS Energy Lett.* **2**, 1214 (2017).
- ³⁸W.-J. Yin, T. Shi, and Y. Yan, *Appl. Phys. Lett.* **104**, 063903 (2014).
- ³⁹W.-J. Yin, J.-H. Yang, J. Kang, Y. Yan, and S.-H. Wei, *J. Mater. Chem. A* **3**, 8926 (2015).
- ⁴⁰A. Walsh, D. O. Scanlon, S. Chen, X. G. Gong, and S.-H. Wei, *Angew. Chem., Int. Ed.* **54**, 1791 (2015).
- ⁴¹D. Shi, V. Adinolfi, R. Comin, M. Yuan, E. Alarousu, A. Buin, Y. Chen, S. Hoogland, A. Rothenberger, K. Katsiev, Y. Losovyj, X. Zhang, P. A. Dowben, O. F. Mohammed, E. H. Sargent, and O. M. Bakr, *Science* **347**, 519 (2015).
- ⁴²O. Almora, "Hysteresis and capacitive features of perovskite solar cells," Ph.D. thesis (Jaume I de Castelló, 2020).